

Supporting Information

Atomically smooth single-crystalline platform for low-loss plasmonic nanocavities

Lufang Liu,^{1,#} Alexey V. Krasavin,^{2,#} Junsheng Zheng,¹ Yuanbiao Tong,¹ Pan Wang,^{1,*} Xiaofei Wu,³ Bert Hecht,³ Chenxinyu Pan,¹ Jialin Li,¹ Linjun Li,¹ Xin Guo,¹ Anatoly V. Zayats,^{2,*} Limin Tong^{1,*}

¹State Key Laboratory of Modern Optical Instrumentation, College of Optical Science and Engineering, Zhejiang University, Hangzhou 310027, China

²Department of Physics and London Centre for Nanotechnology, King's College London, Strand, London WC2R 2LS, U.K.

³NanoOptics & Biophotonics Group, Experimentelle Physik 5, Physikalisches Institut, Universität Würzburg, Am Hubland, 97074 Würzburg, Germany

[#]These authors contributed equally to this work

* W.P.: email, nanopan@zju.edu.cn.

* A.V.Z.: email, a.zayats@kcl.ac.uk.

* L.T.: email, phytong@zju.edu.cn.

Section 1. Synthesis of GMFs.

GMFs were synthesized using a modified wet-chemical method¹. First, a growth solution was prepared by the addition of 90- μL of 0.1 M chloroauric acid (98%, Sigma-Aldrich) aqueous solution into a 10-mL ethylene glycol (99.8%, Sigma-Aldrich) in a 20-mL glass vial. Then, a cleaned glass slide was immersed into the solution at a slightly tilted angle. Finally, the growth solution was heated to 95°C in an oven and kept at this temperature for a certain reaction time defining the dimensions of the resulting GMFs. After the growth, the glass slide with GMFs on the surface was taken out of the growth solution, cleaned with ethanol, and dried in a nitrogen environment for the next-step use. The thickness of GMFs can be tuned from ~ 10 nm to hundreds of nanometers by the control of growth time from ~ 4 to 24 h. As shown in Fig. S1, with the increase of growth time, the size of GMFs increases from ~ 10 μm to hundreds of micrometers. At the same time, there is a gradual change in the colour of GMFs taken both in reflection and transmission, which is due to the increase of the GMF thickness.

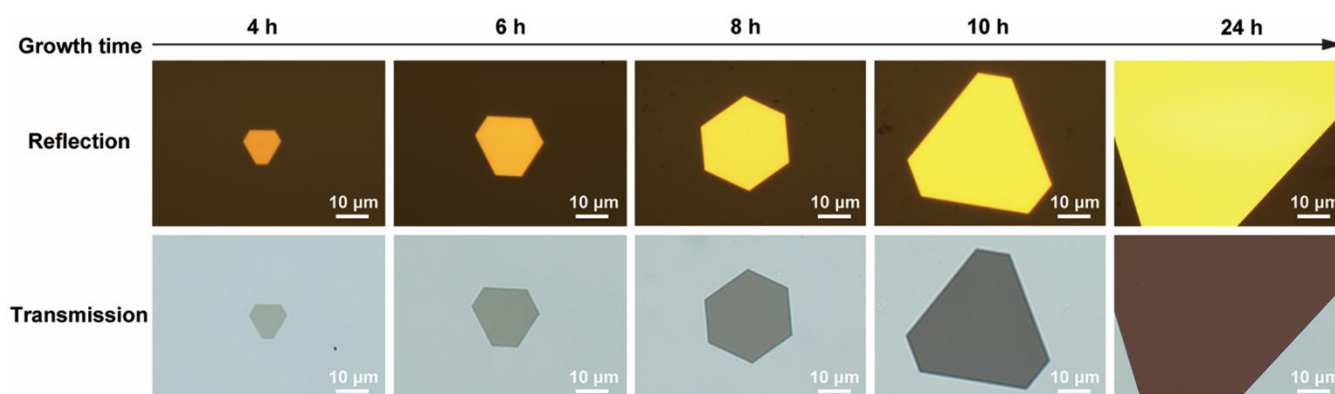


Figure S1. Optical micrographs of GMFs with an increasing growth time from 4 to 24 h. The top panels were taken in reflection, while the bottom panels were taken in transmission.

Section 2. Synthesize of GNRs

GNRs were prepared using a seed-mediated method². Firstly, to prepare the seed solution, an ice-cold NaBH₄ solution (0.6 mL, 0.01 M) was added into a mixture of HAuCl₄ (0.25 mL, 0.01 M) and CTAB (9.75 mL, 0.1 M) aqueous solutions. The resultant solution was rapidly stirred for 2 min and kept at room temperature for 2 h before use. Secondly, the growth solution was made by the sequential addition of HAuCl₄ (2 mL, 0.01 M), AgNO₃ (0.4 mL, 0.01 M), ascorbic acid (0.32 mL, 0.1 M) and HCl (0.8 mL, 1.0 M) aqueous solutions into a CTAB aqueous solution (40 mL, 0.1 M). The obtained solution was mixed by gently shaking. Then 3 μ L seed solution was added to the growth solution. The resultant solution was gently stirred for 20 s and then kept undisturbed overnight. Figure S2A shows a TEM image of as-synthesized GNRs. The average diameter and length are determined to be 52 ± 4 and 103 ± 5 nm, respectively. Figure S2B shows an extinction spectrum of GNRs dispersed in water.

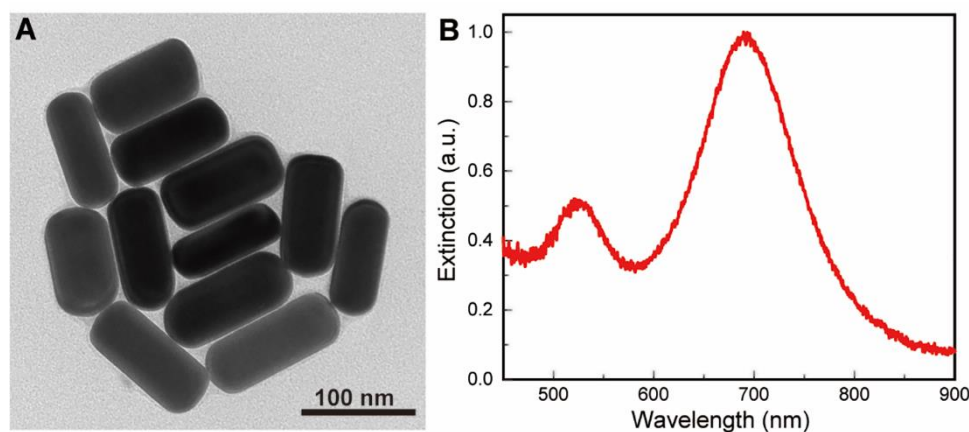


Figure S2. TEM images and extinction spectra. **A**, TEM image of GNRs. **B**, Extinction spectrum of GNRs dispersed in an aqueous solution.

Section 3. Dark-field spectroscopy setup

Scattering of single nanocavities was characterized via a dark-field scattering spectroscopy, as schematically shown in Fig. S3A. Briefly, an unpolarized white light from a halogen tungsten lamp was first focused onto NRoMF nanocavities on a glass slide at an incident angle of 68° by a $100\times$ dark-field objective (NA = 0.8, TU Plan ELWD, Nikon). The scattering light from single NRoMF nanocavities was collected by the same objective and directed with a beam splitter to a charge-coupled device camera (DS-Fi3, Nikon) for imaging and a spectrometer (QE pro, Ocean Insight) for the spectral analysis. All the scattering spectra were measured under the same illuminating condition and integration time. The measured scattering spectra were calibrated by the spectrum of the white light lamp and spectral response of the detection system (Fig. S3B).

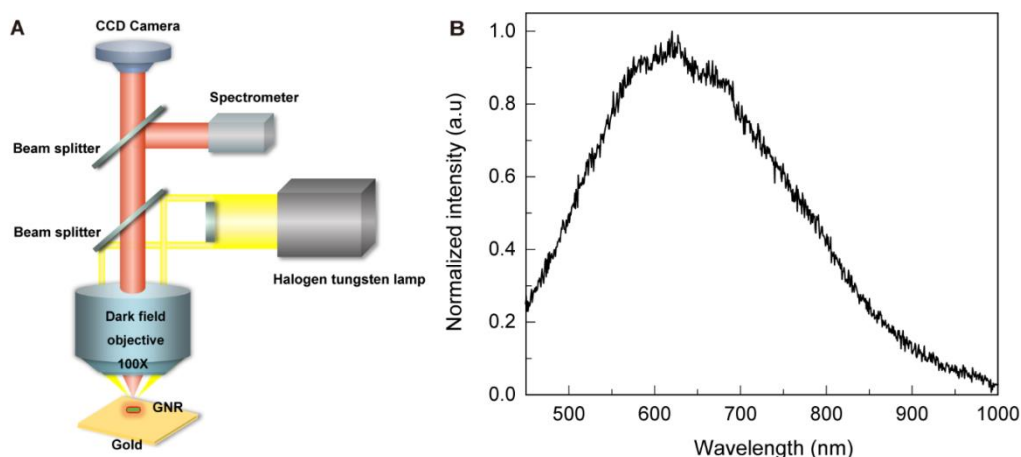


Figure S3. **A**, Schematic diagram of the dark-field spectroscopy setup. **B**, Normalized spectrum of the white light source of the dark-field spectroscopy setup, collected by the detection system, which therefore includes the spectral profile of the white light lamp as well as the spectral response of the detection system.

Section 4. Numerical simulations

The simulations were performed using a finite element method (COMSOL Multiphysics 5.4) in a scattered field formulation. GNRs implemented as elliptically-tapered cylinders matching the geometry of their

experimental counterparts in Fig. 2 and covered with a CTAB layer (1 nm in thickness) were placed with proper spacers (~ 1.2 nm used in simulation, it is reasonable that the thickness of the organic layer on microflakes may decrease when measured with TEM under vacuum) onto a gold slab presenting the microflake lying on a substrate (see Fig. S4 for the structural parameters used in the simulation). The nanostructure was illuminated with a plane wave at 68° . To avoid back-reflection, the simulation domain was surrounded by perfect matched layer. To reduce the numerical complexity of the simulations symmetry of the problem was utilized, which allows modeling of only a half of the overall domain setting appropriate (perfect electric or perfect magnetic conductor) boundary conditions on the slicing boundary, defined by the polarization of the incident wave. The wavelength of the incident wave was varied from 450 to 1000 nm, while the power flow of the scattered fields was integrated in the near-field region 350 nm from the nanorod center and inside a 50° collection angle corresponding to the NA of the objective employed in the experiments. The partial near-field scattering cross-section $\sigma_{\text{scat}}^{\text{NF}}$ was obtained by dividing the obtained integral with the intensity of the incident wave. The refractive indices of gold, CTAB were taken from Refs. 3 and 4, respectively. While the refractive index of single-crystalline optically-thin flakes may deviate from the tabulated values, their thickness dependence will be investigated elsewhere.

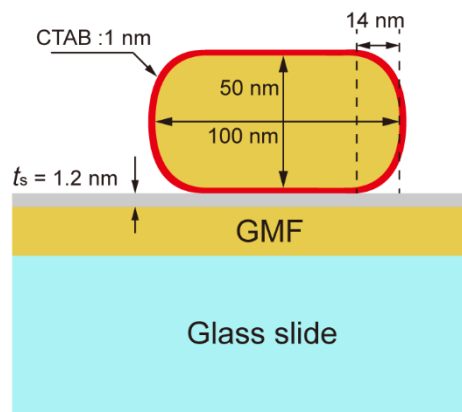


Figure S4. Structural parameters of the nanocavity used for simulation.

Section 5. Formation of modes V_1 and V_2

For a nanosphere-on-mirror nanocavity under TM excitation, a vertically (perpendicular to a mirror) polarized mode (Fig. S5) can be excited due to the coupling of the vertical dipolar mode of the nanosphere with its image dipole in the gold mirror⁵, which has only one hotspot at the center of the gap. When the nanosphere is elongated into a rod shape, in addition to the film-coupled vertical dipolar mode, the nanocavity can also support in this wavelength range nonradiative 3rd-order (3 antinodes) Fabry-Perot resonance in the MIM gap defined by the length of the rod⁶. Thus, the hybridization between the film-coupled vertical dipolar mode and the 3rd-order Fabry-Perot mode forms antibonding and bonding modes (Fig. S6), named modes V_1 and V_2 , respectively.

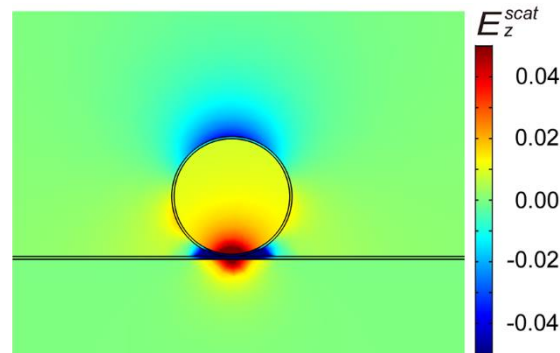


Figure S5. Normalized E_z^{scat} field distribution of film-coupled vertical dipolar mode of a nanocavity formed by a 52-nm-diameter gold nanosphere on a GMF (100 nm in thickness).

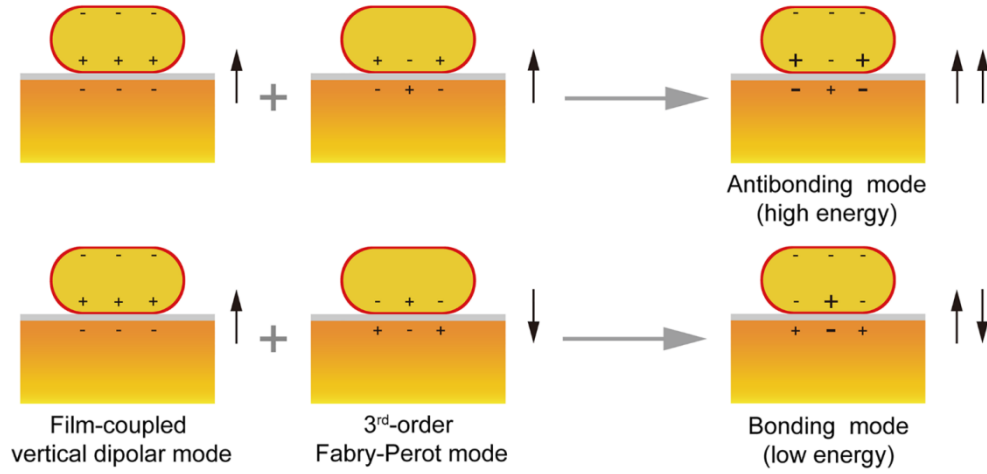


Figure S6. Schematic diagram showing hybridization between film-coupled vertical dipolar mode and 3rd-order Fabry-Perot mode to generate modes V_1 and V_2 .

Section 6. E_x^{scat} field distribution of mode M_2

Figure S7 presents the E_x^{scat} field distribution of mode M_2 of the NRoMF nanocavity investigated in Fig. 2.

Note that the charge maxima of the Fabry-Perot mode correspond to the node of the E_x^{scat} field, so the Fabry-Perot mode in the gap is clearly of the 6th order.

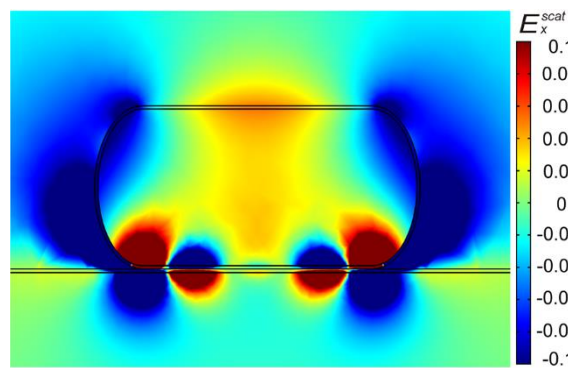


Figure S7. Normalized E_x^{scat} field distribution of mode M_2 of the nanocavity investigated in Fig. 2.

Section 7. Effect of spacer thickness on the optical properties

The effect of spacer thickness on the optical properties of NRoMF nanocavities was investigated by employing an amorphous Al_2O_3 layer as the dielectric spacer. Al_2O_3 thin layers with various thicknesses were deposited on 100-nm-thickness GMFs using atomic layer deposition (ALD, SENTECH SI ALD) at 120 °C. To initiate the first reaction cycle on the GMFs, the surface of the GMFs were hydroxylated by immersing GMF-grown glass slides into a 10 mM 2-mercapto-ethanol (99%, Sigma-Aldrich) ethanol solution overnight. Then the glass slides were rinsed with excessive ethanol and dried with nitrogen for ALD deposition. The thickness of Al_2O_3 spacer layer can be precisely controlled by controlling the reaction cycle. Figure S8 presents TEM images of the edges of Al_2O_3 coated GMFs, clearly showing the thickness of Al_2O_3 layer to be 1.5, 2.4 and 4.0 nm.

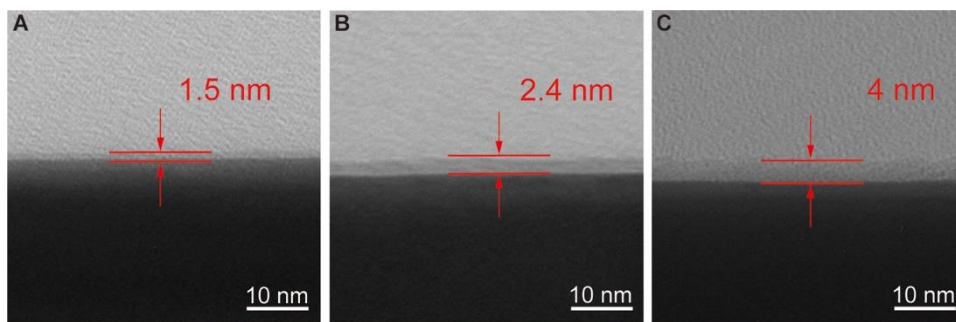


Figure S8. TEM images of the edges of GMFs with different thicknesses of Al_2O_3 layers: (A) 1.5, (B) 2.4 and (C) 4 nm.

When the Al_2O_3 thickness is 1.5 nm, as have been observed in the main text, there are three resonance peaks in the scattering spectrum (Fig. S9, yellow line), located at 550, 610 and 700 nm, respectively. With the further increase of Al_2O_3 thickness to 2.4 and 4.0 nm (green and blue lines), along with the blue-shift of the resonance peaks of modes V_1 and V_2 , a new resonance peak (around 811 and 783 nm, respectively) emerges. This peak corresponds to mode M_4 predicted in Fig. 2C, which now moves into the detection spectral range of the set-up. Simultaneously, the scattering intensity of mode M_4 becomes stronger as the

nanorod dipole and its image in metal get more separated. Accordingly, with the increase of Al_2O_3 thickness, there is a distinct change in the scattering patterns of NRoMF nanocavities (insets of Fig. S9). It should be mentioned that the relatively weak scattering intensity of mode M_4 observed experimentally is mainly due to the chromatic aberration of the optical system⁷.

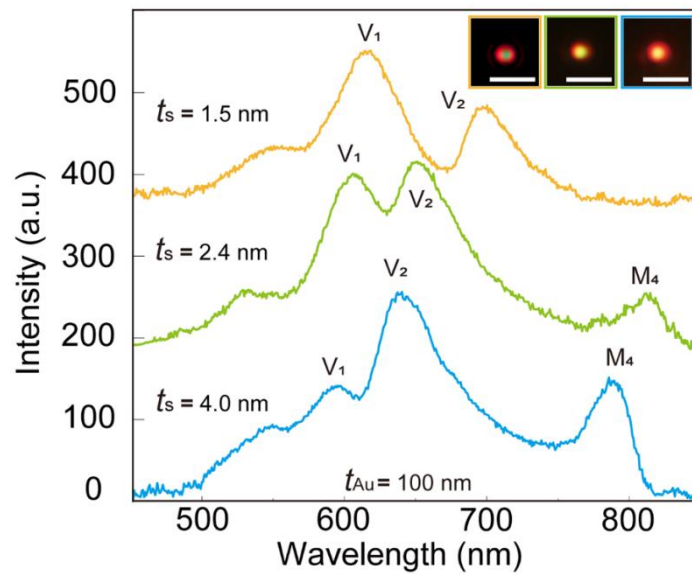


Figure S9. Scattering spectra of NRoMF nanocavities formed on 100-nm-thickness GMFs with varying Al_2O_3 thickness t_s of 1.5, 2.4 and 4.0 nm. Insets: corresponding dark-field scattering images of the measured nanocavities. Scale bar is 2 μm .

Section 8. Transmittance of GMFs with different thicknesses

The transmittance of GMFs was measured with a white light focused in the center of a GMF under an optical microscope. As shown in Fig. S10, with the decrease of a GMF thickness, the transmittance of GMFs increases gradually from 25% to 48% and 70% at the wavelength of 510 nm.

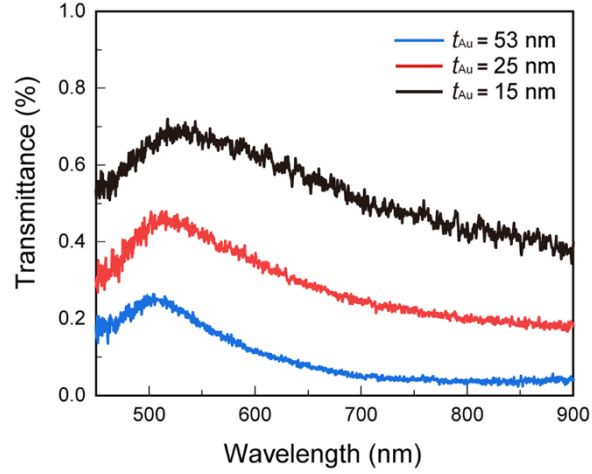


Figure S10. Transmittance of GMFs with thicknesses of 53, 25 and 15 nm, respectively.

Section 9. Scattering cross-sections and field distributions of nanocavities on GMFs with various thicknesses

Figure S11 presents calculated scattering cross-sections of NRoMF nanocavities formed on GMFs with thicknesses of 100, 53, 25, 15 and 6 nm, respectively. The corresponding normalized E_z^{scat} field distributions of modes M_2 , M_4 , V_1 and V_2 of NRoMF nanocavities are further shown in Fig. S12.

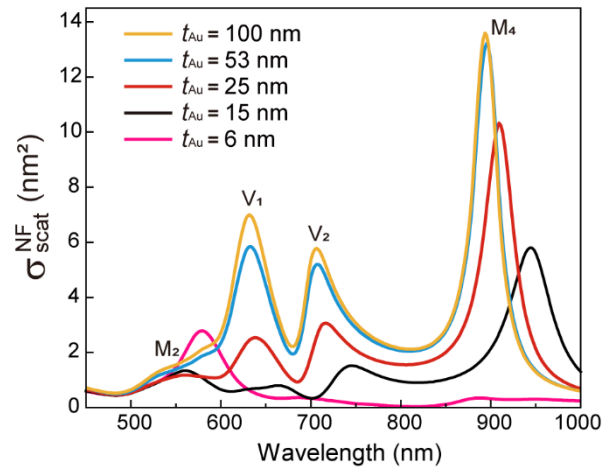


Figure S11. Calculated σ_{scat}^{NF} for NRoMF nanocavities formed on GMFs with thicknesses of 100, 53, 25, 15 and 6 nm, respectively.

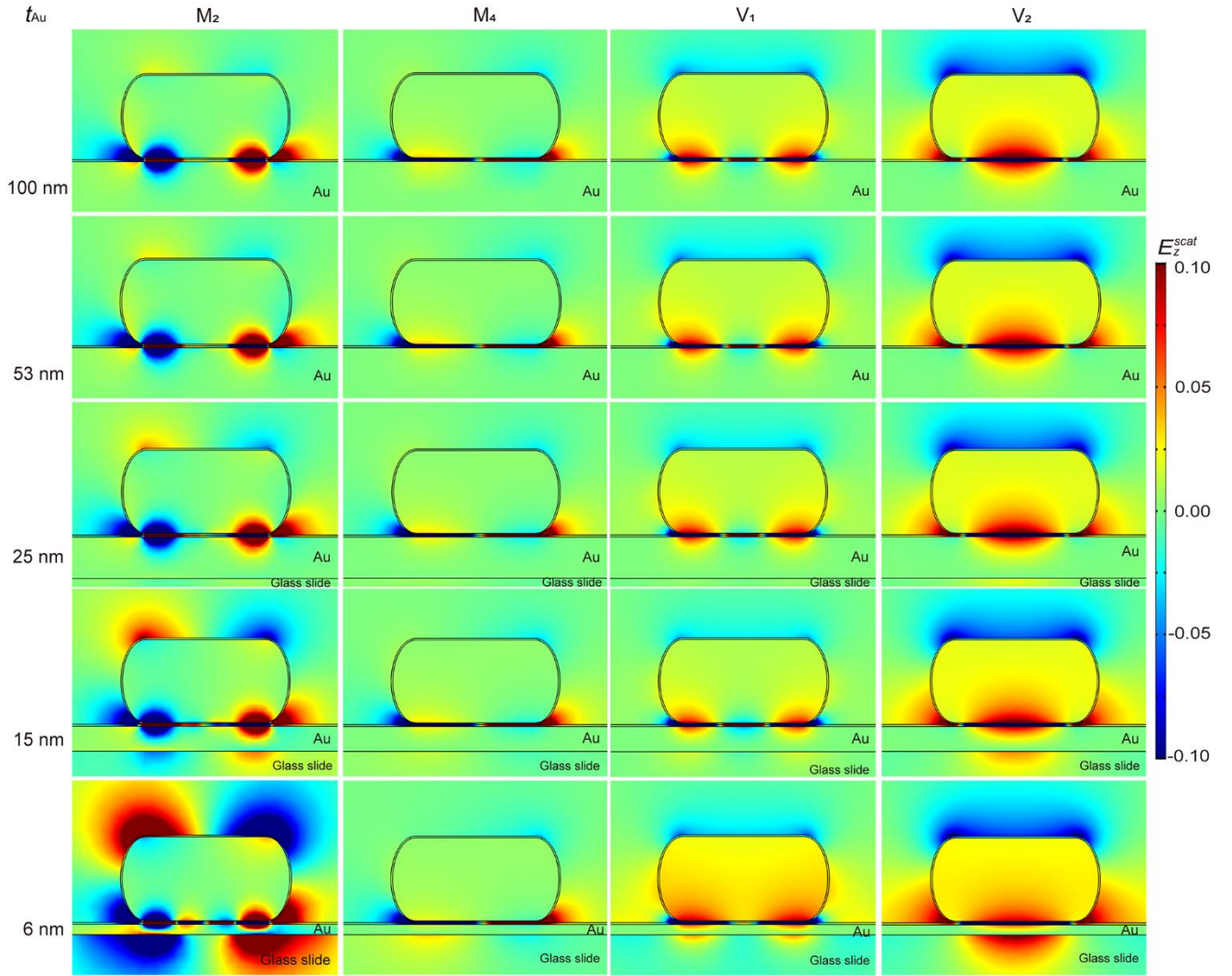


Figure S12. Normalized E_z^{scat} field distributions of modes M_2 , M_4 , V_1 and V_2 for NRoMF nanocavities, as indicated in Fig. S11, with t_{Au} of 100, 53, 25, 15 and 6 nm.

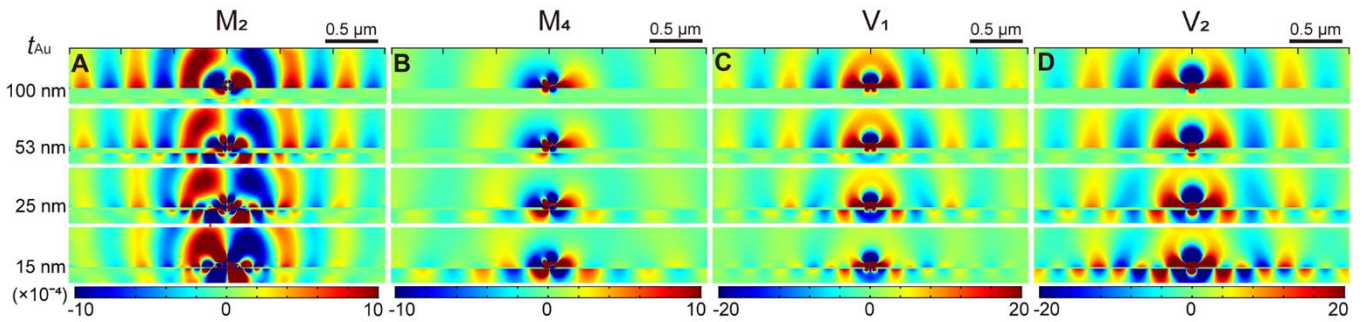


Fig. S13. Spatial distributions of normalized E_z^{scat} field at the resonance peaks of modes M_2 , M_4 , V_1 and V_2 in the x - z plane for the nanocavities formed on the GMFs of various thicknesses under TM_1 excitation.

Figure S13 shows the calculated spatial distributions of normalized E_z^{scat} field at the resonance peaks of modes M_2 , M_4 , V_1 and V_2 in the x - z plane. As can be seen on the field distributions, in addition to couple into free space as photons, the excited plasmonic modes in NRoMF nanocavities can also couple into the GMF as propagating SPPs^{8,9}. At large thicknesses (e.g., 100 nm) the NRoMF modes are coupled to the SPP mode at the gold-air interface. With the decrease of GMF thickness, SPPs propagating at the gold-air and gold-silica interfaces are coupled and form a highly-confined short-range IMI propagating mode^{10,11}, so the NRoMF modes may couple to it. For mode M_2 with a resonance at short wavelength, the short-range IMI mode is excited with low efficiency and can be observed only in the close vicinity of the nanocavity (Fig. S13A, bottom two panels) as in this spectral range the SPP is extremely lossy. On the other hand, for mode M_4 positioned at much larger wavelength, the short-range IMI SPP mode is excited by NRoMF with higher efficiency due to a better mode overlap and can propagate for a longer distance (Fig. S13B, bottom panel) as the loss in this spectral range is lower. Analogous situation is observed for the case of vertically oriented resonances (Fig. S13C,D).

Section 10. Deposition and characterization of gold films

Gold films were prepared by thermal evaporation (Nano36, Kurt J. Lesker). Thermal annealing of evaporated gold films is an effective way to further improve the film quality by increasing grain sizes^{12,13}, which can, therefore, reduce the scattering of electrons at grain boundaries¹⁴. Annealing is known to usually roughen the surface. When combined with the template-stripping approach, it can greatly improve the surface quality (by using the surface in contact with the substrate) as well¹². However, the rough surface at the opposite side would still affect the optical performance of nanocavities when the film is optically thin. Additionally, it is difficult to apply thermal annealing (requiring high temperature, e.g., 500 °C) and/or

template-stripping approaches onto other optical devices or systems for the integration of nanocavities. Therefore, for thin films which are the main focus of the manuscript, it is reasonable to use thermally deposited gold films as a mirror for the comparison in Fig. 4.

To avoid the use of metallic adhesion layers (such as Cr, Ti) that can introduce significant optical loss to plasmonic structures¹⁵, cleaned glass slides were first functionalized with a monolayer of (3-Aminopropyl)trimethoxysilane instead for the subsequent deposition of gold. This was realized by immersing them into a 5 mM (3-Aminopropyl)trimethoxysilane (97%, Sigma-Aldrich) ethanol solution overnight and kept at 80 °C for 1 h to enhance the attachment of (3-Aminopropyl)trimethoxysilane molecules on the glass slide surface. The functionalized glass slides were rinsed with excessive ethanol and dried with nitrogen. Gold films with different thicknesses were deposited in vacuum ($\sim 10^{-6}$ Torr) on the prepared glass slides at a rate of 1 Å/s. Figure S14 shows SEM images of the surface of a GMF and deposited films with thicknesses of 15 and 53 nm, respectively. Figure S15 (and Figures 4A and 4B) presents AFM images of the surface of a GMF and deposited gold films. The superior surface quality of GMFs over the deposited gold films can be clearly seen.

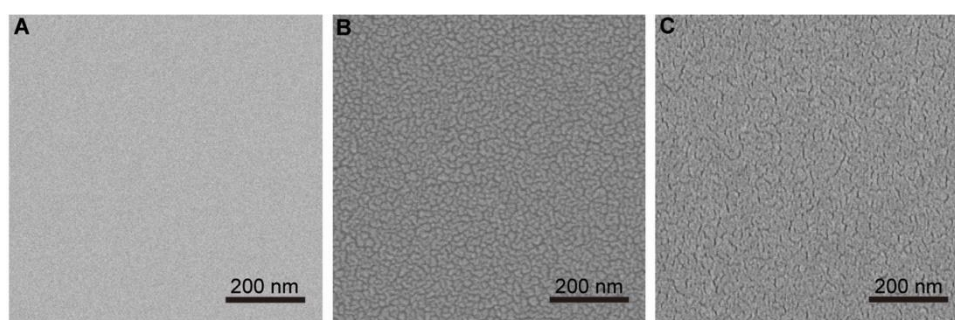


Figure S14. SEM images of GMF and deposited gold films. **A**, SEM image of 15-nm-thickness GMF with atomic-level surface roughness. **B**, **C**, SEM images of deposited gold films with t_{Au} of **(B)** 15 and **(C)** 53 nm.

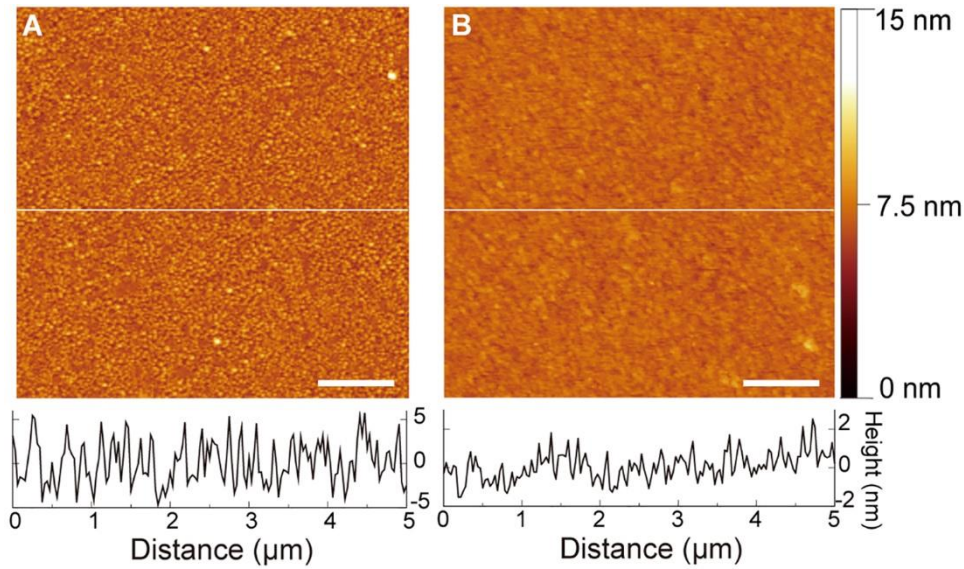


Figure S15. AFM images of the surface of thermally-deposited gold films with thicknesses of (A) 25 and (B) 53 nm with the RMS roughness of 2.7 and 1.4 nm, respectively.

Section 11. Comparison of quality factors

The quality factors (Q factors) of modes V_1 and V_2 were extracted from the scattering spectra as follows: the scattering spectra were first plotted in the frequency domain, then the obtained dependences were fitted with sums of Lorentzian line shapes describing the resonances (modes V_1 , V_2 , M_1 , M_2 and M_3), as shown in Fig. S16 (presenting the example of fitting the frequency-domain spectrum of a nanocavity formed on a 53-nm-thickness GMF). The yellow and green lines show the fitted resonances for modes V_1 and V_2 , while the overall sum (including modes M_1 , M_2 and M_3) presented by the red line demonstrates an excellent fit of the experimental data. Then, the resonance frequency (ω) and full-width at half-maximums (FWHM) of each modes were taken from the output fitted values. Finally, the Q factors of the modes were determined as the ratios of ω to FWHM. The Q factors of modes V_1 and V_2 of scattering spectra for GMF-based and deposited film-based NPoM nanocavities with various mirror thicknesses (shown in Figs. 4C-4E and Fig.

S17) are shown in Table S1. The Q factors of modes V_1 and V_2 in the calculated results (shown in Fig. 3K) are presented as well in the table for comparison.

As shown in Table S1, the Q factors of modes V_1 and V_2 for GMF-based nanocavities are higher than those of deposited film-based NPoM nanocavities. When the mirror thickness is around 100 nm, the scattering intensities and Q factors of modes V_1 and V_2 of the GMF-based nanocavity are only slightly higher than those of their GMF-based counterpart. This is logical due to the improved surface quality for 100-nm-thickness gold film and the relatively large contribution of radiative scattering loss to the total loss for modes V_1 and V_2 . However, when the mirror thickness is decreased to 25 or 15 nm, the Q factors of modes V_1 and V_2 for GMF-based nanocavities are about twice the values of deposited film-based nanocavities, which is due to the low quality of the optically-thin deposited gold films. We can also see that benefitted from the single-crystalline structure and excellent surface smooth of GMFs (with thickness down to 15 nm), the Q factors of modes V_1 and V_2 of the GMF-based nanocavities are quite close to the theoretical limit values, which are determined by the inevitable Ohmic loss and radiative damping.

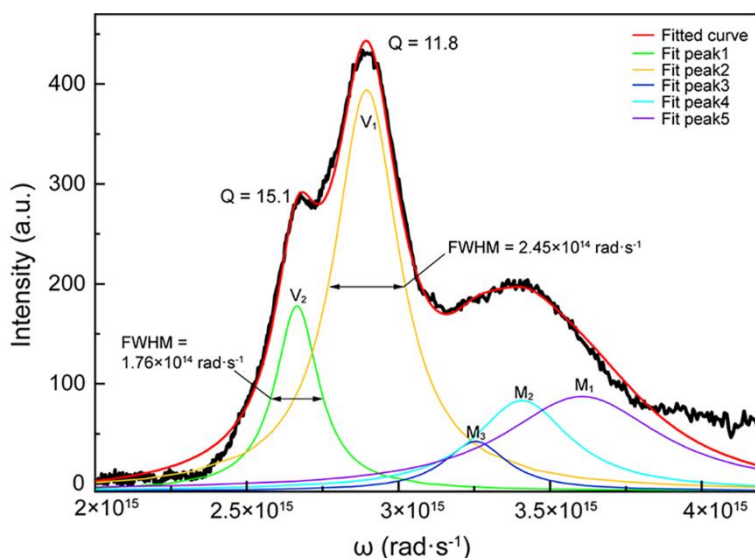


Figure S16. The frequency-domain scattering spectrum of the nanocavity formed on a GMF with t_{Au} of 53 nm. The color lines present resonances for different modes fitted with Lorentzian line shapes.

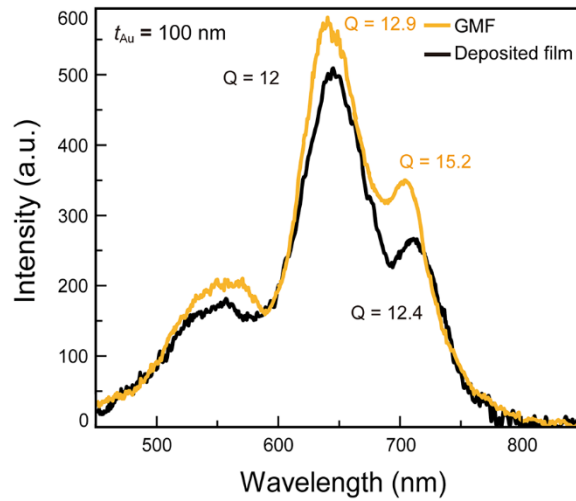


Figure S17. Scattering spectra of the nanocavities formed on a gold film and a GMF with the same thickness (t_{Au}) of 100 nm, respectively. The quality factors of modes V_1 and V_2 are labeled correspondingly.

Table S1 Comparison of Q factors of modes V_1 and V_2 of scattering spectra for GMF and deposited film-based nanocavities as well as the calculated results.

	$t_{Au} = 100$ nm		$t_{Au} = 53$ nm		$t_{Au} = 25$ nm		$t_{Au} = 15$ nm	
	V_1	V_2	V_1	V_2	V_1	V_2	V_1	V_2
Deposited gold film	12	12.4	8.9	10.2	6.9	10.4	/	9.2
GMF	12.9	15.2	11.8	15.1	13.9	15.3	/	15.2
Calculated	13.8	15.1	13.5	15.2	14.0	15.5	/	15.3

Section 12. Transfer of GMFs onto an angled fiber

The chemically synthesized GMFs are movable, and thus can be readily transferred onto other substrates via a polydimethylsiloxane (PDMS)-mediated approach. As schematically shown in Fig. S18, a GMF grown on a glass slide was first picked up by a clean PDMS thin film, and then an angled fiber was aligned to make a

contact with the GMF on the PDMS film. Finally, the PDMS film was moved away carefully, and the GMF was left on the polished surface of the angled fiber.

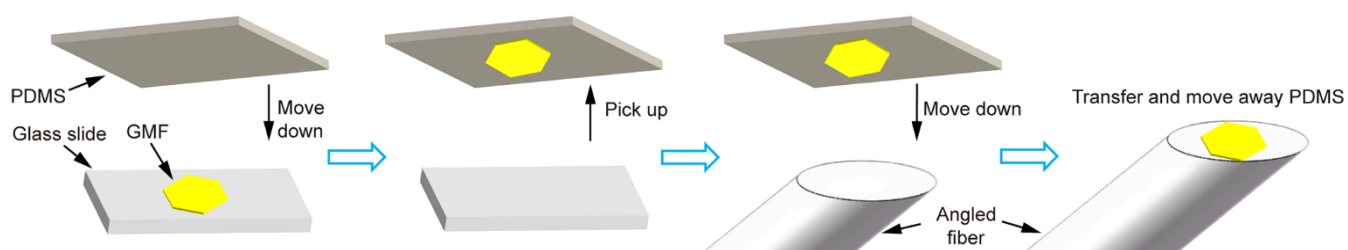


Figure S18. PDMS-mediated transfer of a GMF onto the polished surface of an angled fiber.

Section 13. Integration with an optical microfiber

NRoMF nanocavities can also be readily integrated with a silica microfiber, and excited by the evanescent field of the waveguided light. Silica microfiber, with a diameter of 20 μm , was fabricated by flame-assisted taper drawing from a standard optical fiber¹⁶. Using the method described in Section 12, a GMF with a thickness of ~ 20 nm and a lateral size of 27 μm was transferred onto the sidewall of the silica microfiber. Subsequently, GNRs were deposited onto the GMF by drop-casting to obtain sparsely dispersed NRoMF nanocavities.

References

1. Krauss, E.; Kullock, R.; Wu, X.; Geisler, P.; Lundt, N.; Kamp, M.; Hecht, B., Controlled growth of high-aspect-ratio single-crystalline gold platelets. *Cryst. Growth Des.* **2018**, *18* (3), 1297-1302.
2. Wang, P.; Zhang, L.; Xia, Y.; Tong, L.; Xu, X.; Ying, Y., Polymer nanofibers embedded with aligned gold nanorods: a new platform for plasmonic studies and optical sensing. *Nano Lett.* **2012**, *12* (6), 3145-3150.

3. Olmon, R. L.; Slovick, B.; Johnson, T. W.; Shelton, D.; Oh, S.-H.; Boreman, G. D.; Raschke, M. B., Optical dielectric function of gold. *Phys. Rev. B* **2012**, *86* (23), 235147.
4. He, J.; Unser, S.; Bruzas, I.; Cary, R.; Shi, Z.; Mehra, R.; Aron, K.; Sagle, L., The facile removal of CTAB from the surface of gold nanorods. *Colloids Surf. B* **2018**, *163*, 140-145.
5. Chikkaraddy, R.; Zheng, X.; Benz, F.; Brooks, L. J.; de Nijs, B.; Carnegie, C.; Kleemann, M.-E.; Mertens, J.; Bowman, R. W.; Vandenbosch, G. A. E.; Moshchalkov, V. V.; Baumberg, J. J., How ultranarrow gap symmetries control plasmonic nanocavity modes: from cubes to spheres in the nanoparticle-on-mirror. *ACS Photonics* **2017**, *4* (3), 469-475.
6. Sugimoto, H.; Yashima, S.; Fujii, M., Hybridized plasmonic gap mode of gold nanorod on mirror nanoantenna for spectrally tailored fluorescence enhancement. *ACS Photonics* **2018**, *5* (8), 3421-3427.
7. de Nijs, B.; Bowman, R. W.; Herrmann, L. O.; Benz, F.; Barrow, S. J.; Mertens, J.; Sigle, D. O.; Chikkaraddy, R.; Eiden, A.; Ferrari, A.; Scherman, O. A.; Baumberg, J. J., Unfolding the contents of sub-nm plasmonic gaps using normalising plasmon resonance spectroscopy. *Faraday Discuss.* **2015**, *178* (0), 185-193.
8. Rodríguez-Fortuño, F. J.; Marino, G.; Ginzburg, P.; O'Connor, D.; Martínez, A.; Wurtz, G. A.; Zayats, A. V., Near-field interference for the unidirectional excitation of electromagnetic guided modes. *Science* **2013**, *340* (6130), 328-330.
9. O'Connor, D.; Ginzburg, P.; Rodríguez-Fortuño, F. J.; Wurtz, G. A.; Zayats, A. V., Spin-orbit coupling in surface plasmon scattering by nanostructures. *Nat. Commun.* **2014**, *5* (1), 5327.
10. Economou, E. N., Surface plasmons in thin films. *Phys. Rev.* **1969**, *182* (2), 539-554.
11. Burke, J. J.; Stegeman, G. I.; Tamir, T., Surface-polariton-like waves guided by thin, lossy metal films. *Phys. Rev. B* **1986**, *33* (8), 5186-5201.

12. Nagpal, P.; Lindquist, N. C.; Oh, S.-H.; Norris, D. J., Ultrasmooth patterned metals for plasmonics and metamaterials. *Science* **2009**, *325* (5940), 594-597.
13. Nogues, C.; Wanunu, M., A rapid approach to reproducible, atomically flat gold films on mica. *Surf. Sci.* **2004**, *573* (3), L383-L389.
14. Kuttge, M.; Vesseur, E. J. R.; Verhoeven, J.; Lezec, H. J.; Atwater, H. A.; Polman, A., Loss mechanisms of surface plasmon polaritons on gold probed by cathodoluminescence imaging spectroscopy. *Appl. Phys. Lett.* **2008**, *93* (11), 113110.
15. Habteyes, T. G.; Dhuey, S.; Wood, E.; Gargas, D.; Cabrini, S.; Schuck, P. J.; Alivisatos, A. P.; Leone, S. R., Metallic adhesion layer induced plasmon damping and molecular linker as a nondamping alternative. *ACS Nano* **2012**, *6* (6), 5702-5709.
16. Tong, L.; Gattass, R. R.; Ashcom, J. B.; He, S.; Lou, J.; Shen, M.; Maxwell, I.; Mazur, E., Subwavelength-diameter silica wires for low-loss optical wave guiding. *Nature* **2003**, *426* (6968), 816-819.